

VISUALIZATION OF ACOUSTIC PRESSURE AND VELOCITY PATTERNS WITH PHASE INFORMATION IN THE PINNA CAVITIES AT NORMAL MODES

Parham Mokhtari, Hironori Takemoto, Ryouichi Nishimura and Hiroaki Kato

National Institute of Information and Communications Technology (NICT),
3-5 Hikaridai, Seikacho, “Keihanna Science City”, Kyoto 619-0289, Japan

ABSTRACT

As the peaks of head-related transfer functions are generated by normal modes of the pinna (external ear), the peak center-frequency and the three-dimensional pattern of each normal mode depend on individual pinna geometry. Traditionally, normal modes are visualized mainly in terms of pressure anti-nodes. To better understand the relations between the acoustics and geometry of pinnae, in this study we describe computational methods that extend previous visualizations: (i) by including *principal vectors of velocity* that reveal patterns of energy exchange between anti-nodes and energy loss to the surrounding air, and (ii) by enabling separate visualization of resonance patterns with *common phase-angles*. These methods are applied to two individual pinnae: one with a standard set of normal modes, and one whose second and third normal modes are confusable.

Index Terms— pinna, normal mode, visualization

1. INTRODUCTION

Humans can localize sounds in three-dimensional (3D) space owing to head-related transfer functions (HRTFs), which are characterized by spectral peaks and notches. As HRTF peaks are acoustic *normal modes* of the human pinna (external ear), their center-frequencies depend on individual pinna geometry. A better understanding of the relations between the acoustics and geometry of the pinna is pivotal for applications such as HRTF personalization for 3D audio, where it is beneficial to know the pinna measurements that are most relevant to each peak. A key to such knowledge, is effective visualization of the normal mode (or resonance pattern) associated with each peak.

The earliest attempt at such visualization involved laborious measurements of sound pressure amplitudes and relative phases within the pinna cavities [1]. More recently, computer simulation methods have enabled more detailed visualizations of the distributions of absolute pressure on the pinna surface [2], patterns of acoustic sensitivity to pinna surface perturbations [3], and pressure nodes and anti-nodes within pinna cavities [4]. These studies have confirmed that in general for a meatus-blocked pinna, the first peak (P1) corresponds to a quarter-wavelength lateral resonance of the

concha (along its depth), while the second and higher peaks (P2, P3, ...) correspond to “vertical” resonance modes with an increasing number of pressure anti-nodes (or equivalently, regions of high sensitivity) distributed in the pinna cavities.

Based on such knowledge, our analysis of the left and right pinnae of ten individuals yielded a quantitative model to estimate P1 from depth-related pinna measurements [5]. However, the development of estimation models for P2 and higher peaks is hampered by an incomplete understanding of what kind of “vertical” measurements are required to estimate these peaks for a variety of pinna geometries.

To gain a better understanding, it is vital to develop more advanced methods for visualization of pinna normal modes. This paper introduces new methods based on signal processing of the pressure and particle-velocity waveforms calculated by acoustic simulation. In particular, we describe: (i) visualization of the 3D field of principal velocity vectors, revealing the oscillatory exchange of acoustic energy among pressure anti-nodes, as well as the loss of energy to the surrounding air; and (ii) calculation and thresholding of relative phase-angles among pressure and velocity signals, to separate independent resonances associated with one peak. We apply these methods first to a pinna with unambiguous normal modes, and then to a pinna whose second and third peaks present an interpretative challenge.

2. PINNA GEOMETRY & ACOUSTIC SIMULATION

The head geometries of an adult male and an adult female were measured by magnetic resonance imaging (MRI) with a Siemens 3T “Magnetom Trio” installed at the Brain Activity Imaging Center at ATR Promotions Inc., and contiguous head volumes were segmented from the surrounding air [6]. As HRTF peaks are caused by the pinna and are therefore essentially the same as the peaks on pinna-related transfer functions (PRTFs) [3][4], for computational efficiency a smaller volume containing only the right pinna and a patch from the side of the head was extracted, as shown in Fig. 1.

A finite-difference time domain (FDTD) acoustic simulator was used to calculate the pressure and particle-velocity sound fields in response to a broadband point source placed adjacent to the center of the blocked ear-canal (within the cavum concha). Representing the volume on a 3D Cartesian grid with resolution 0.2 cm allowed calculation

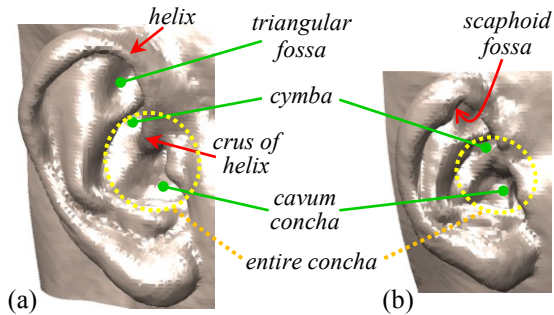


Figure 1. Right pinna of an adult (a) male and (b) female, shown approximately on the same scale.

of transfer functions up to 14 kHz. With each pinna volume surrounded by an optimal perfectly matched layer [7], farfield pressure responses were calculated [8] at 1250 spatial locations (25 azimuth \times 50 elevation angles [9]) a distance 1 m from the head center. We have previously shown that HRTFs calculated in this way from a manikin's 3D head geometry matched closely with those obtained from independent acoustic measurements [10].

For visualization of the normal modes, pressure and velocity responses of duration 3 ms were calculated at all voxels of air within a sub-volume enclosing each pinna. After measuring the center-frequencies of PRTF peaks (in section 3), every pressure and velocity time-waveform within the sub-volume was bandpass filtered at each of those frequencies, with zero phase distortion. These filtered signals, representing the pressure and velocity responses at each resonance, were used for the calculation of derived acoustic quantities useful for visualization of the normal mode corresponding to each peak (in section 4).

3. PINNA-RELATED TRANSFER FUNCTION PEAKS

Median-plane PRTFs calculated for each pinna are shown in Fig. 2 (top). In addition to notches whose frequencies vary with elevation angle, six and four peaks, respectively, of relatively constant frequency are apparent. Owing to the peaks' stability, representative values can often be measured on the mean transfer function [5]. Indeed, the male pinna's six peak center-frequencies were measured on the mean PRTF (Fig. 2a): P1 at 4.1 kHz, P2 at 6.1 kHz, P3 at 8.7 kHz, P4 at 10.9 kHz, P5 at 12.3 kHz, and P6 at 13.9 kHz.

However for the female pinna, the second peak did not appear in the overall mean PRTF (solid line in Fig. 2b), due to the presence of a deep notch at the same frequency at low elevations. Therefore, as shown by the dashed line in Fig. 2b, this directional second peak was measured on the mean of PRTFs at only high elevations ($-45^\circ \leq$ azimuth angle $\leq 45^\circ$, and $45^\circ \leq$ elevation angle $\leq 135^\circ$). All four peak center-frequencies of the female pinna could thus be measured: P1 at 4.8 kHz, P2 at 7.4 kHz, P3 at 8.9 kHz, and P4 at 11.7 kHz.

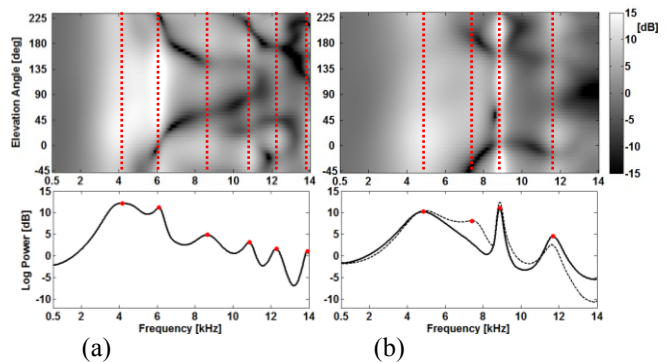


Figure 2. Top panels: median-plane PRTFs of the (a) male and (b) female pinnae, with peaks indicated by dashed red lines. Lower panels: the corresponding pinna's mean PRTFs. Solid lines: mean PRTF over all 1250 spatial locations, with peaks marked by red circles. Dashed black line: mean of PRTFs at only high elevations, with P2 marked by a red circle.

4. VISUALIZATION OF PINNA NORMAL MODES

Here we first describe the methods involved in visualizing the pressure and velocity sound fields (section 4.1); we then apply the methods to reveal standard normal modes of the male pinna (section 4.2), and to disambiguate the second and third normal modes of the female pinna (section 4.3).

4.1. Signal processing methods

The two quantities calculated by FDTD simulation at every discrete time-step t and position \mathbf{x} in the pinna sub-volume, are acoustic pressure $p(\mathbf{x}, t)$ and particle-velocity vector $\mathbf{v}(\mathbf{x}, t)$. Two useful acoustic quantities that can be derived from p and \mathbf{v} , are the *potential* and *kinetic energy densities*:

$$PED(\mathbf{x}, t) = p^2(\mathbf{x}, t) / (2\rho_0 c^2) \quad (1)$$

$$KED(\mathbf{x}, t) = \mathbf{v}(\mathbf{x}, t) \cdot \mathbf{v}(\mathbf{x}, t) \rho_0 / 2 \quad (2)$$

where c is sound speed and ρ_0 is equilibrium density. For example, we have recently shown [11] that a 3D acoustic *sensitivity map* of a pinna can be calculated by the difference $\langle PED \rangle - \langle KED \rangle$, where $\langle \bullet \rangle$ denotes a time-average.

The spatial distribution of the *time-averaged* $\langle PED \rangle$ is useful for visualizing pressure anti-nodes, because $\langle PED \rangle$ is locally maximum at anti-nodes. However, $\langle PED \rangle$ alone does not include phase information. We consider relative phases by first defining a reference position \mathbf{x}_{pref} close to a $\langle PED \rangle$ maximum (i.e., at a pressure anti-node), then calculating the coefficient of linear correlation r_p between the pressure signal at every position $p(\mathbf{x}, t)$ and that at the reference position $p(\mathbf{x}_{\text{pref}}, t)$. At each position, the *sign* of r_p is carried over to $\langle PED \rangle$, which can then be visualized on the pinna surface with red/blue colors indicating positive/negative phase and color intensity indicating the magnitude of $\langle PED \rangle$.

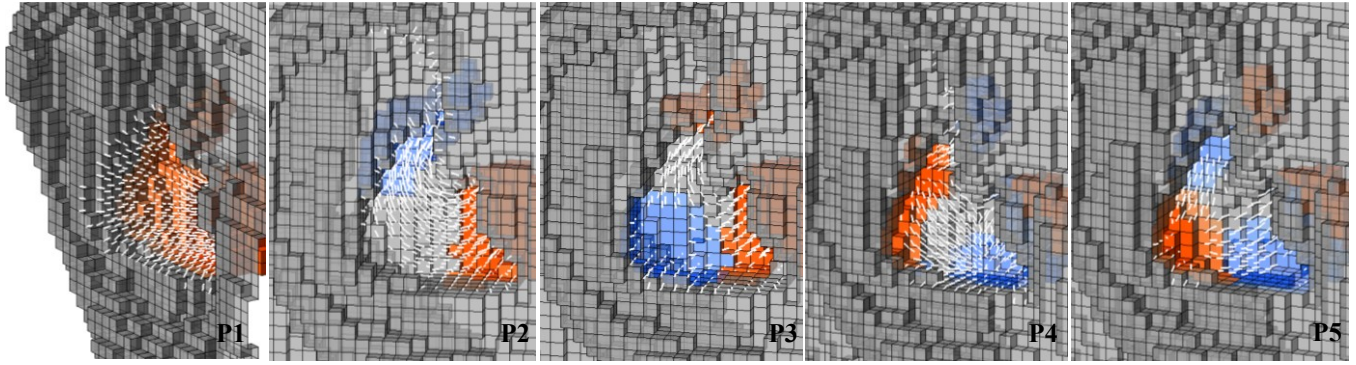


Figure 3. The first five normal modes of the male pinna, corresponding to PRTF peaks P1..P5 in Figs. 2a. Colors indicate surface-patterns of *pressure anti-nodes* with relative phase (red: +, blue: -); white line-strokes indicate *principal vectors of velocity*. To reduce clutter, only vectors with $\sigma_1 > 0.2$ of the max are displayed; $\langle PED \rangle$ was thresholded similarly to enhance the clarity of anti-nodes.

To further clarify the relationships among anti-nodes, it would be useful to concurrently visualize the 3D acoustic flow in the space between them. Of course, the dynamics of acoustic flow can be visualized in a movie showing the time-course of velocity vectors in the sound field. However, our aim here is to capture the essential features of an oscillating vector — i.e., its strength and principal axis at every position — in order to visualize a normal mode in one diagram. As a resonating sound field is characterized by reciprocal movements of air, it is reasonable to apply principal components analysis (PCA) to the time-varying oscillations of the velocity vector $\mathbf{v}(\mathbf{x}, t)$ at each position, in order to obtain the strength σ_1 (square-root of largest eigenvalue) and principal axis (corresponding eigenvector) of the oscillations. The velocity sound field can then be visualized by drawing at each position a short line-segment, oriented along the principal axis and with length proportional to σ_1 .

We also consider relative phases of velocity vectors, by first calculating the time-varying scalar values $v_1(\mathbf{x}, t)$ of all the velocity vectors $\mathbf{v}(\mathbf{x}, t)$ projected onto their respective principal axis. Defining a reference position \mathbf{x}_{ref} close to a $\langle KED \rangle$ maximum (i.e., at a velocity anti-node), we then calculate the absolute value of the coefficient of linear correlation $|r_v|$ between the $v_1(\mathbf{x}, t)$ signal at each position and the $v_1(\mathbf{x}_{\text{ref}}, t)$ signal at the reference position (the absolute value is taken because the polarity of the first eigenvector obtained at any position, and therefore of v_1 , is arbitrary).

The correlations r_p and $|r_v|$ can be transformed to a *difference in phase angle* between the respective pressure or velocity signals, by taking their inverse cosine:

$$\phi_p(\mathbf{x}, \mathbf{x}_{\text{pref}}) = \arccos(r_p) \quad (3)$$

$$\phi_v(\mathbf{x}, \mathbf{x}_{\text{vref}}) = \arccos|r_v| \quad (4)$$

Thus in Eq. 3, correlations of +1, 0, and -1 map respectively to 0° , 90° , and 180° phase difference between $p(\mathbf{x}, t)$ and the reference $p(\mathbf{x}_{\text{pref}}, t)$; in Eq. 4, correlations of +1 and 0 map respectively to 0° and 90° phase difference between $v_1(\mathbf{x}, t)$ and the reference $v_1(\mathbf{x}_{\text{vref}}, t)$. These phase-angle differences ϕ_p and ϕ_v can be thresholded in order to retain and visualize

only the subset of pressure anti-nodes and velocity vectors, respectively, that have a *common phase*.

4.2. A standard set of normal modes

Pinna normal modes are often observed with n anti-nodes (or positive-sensitivity regions) for the n^{th} peak P_n [1][4][11]. This standard sequence is confirmed in our analysis of the male pinna, as shown by the five normal modes in Fig. 3. The proportion of the total variance accounted for by the first principal component of velocity vectors was 93%, 84%, 89%, 87%, and 87% respectively for P1..P5. These results confirm that σ_1 and the first eigenvector define well the strength and principal axis respectively, of oscillations at each position. To reduce clutter, only the vectors with a σ_1 value greater than 0.2 of the maximum are visualized here.

As shown in Fig. 3, the normal mode for P1 has one pressure anti-node covering the entire concha base, and the principal velocity vectors confirm the lateral oscillations of this concha-depth resonance. As discussed by previous authors [1] and here confirmed visually, the relatively broad bandwidth of P1 (cf. Fig. 2) is caused by rapid energy loss due to efficient acoustic coupling with the surrounding air. The P2 normal mode has two anti-nodes of opposing phase, in the cavum concha and cymba (which form deep cavities, visible only by reducing the surface opacity in these figures). The P2 principal vectors follow a 3D curved path between the anti-nodes, partially crossing over the crus of helix; additionally, some vectors point outward from the rim of the concha back-wall and helix, indicating the main locations of energy loss to the surrounding air. The P3, P4, and P5 normal modes have three, four, and five anti-nodes respectively, arranged with alternating phase along the curved path from the cavum concha to the cymba. Their principal vectors indicate energy exchange only between adjacent anti-nodes along that path. For P3 and P5, energy is lost to the surrounding air mainly from the anti-node in the rounded back-corner of the concha; for P4, energy is lost mainly from the concha floor and from the upper parts of the cymba and triangular fossa.

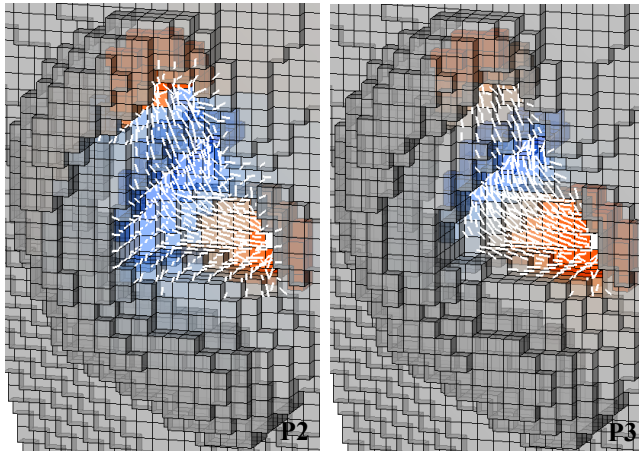


Figure 4. Normal modes for P2 (left) and P3 (right) of the female pinna. Both modes have three pressure anti-nodes, and a generally similar pattern of principal velocity-vectors.

4.3. A normal mode with independent resonances

Similar analysis of the female pinna revealed an interesting case, where the normal modes for both P2 and P3 showed the same number and relative phases of anti-nodes (Fig. 4). The P2 anti-nodes appear in the anterior part of the cavum concha (with positive phase), along the concha back wall extending up to the cymba and part of the triangular fossa (negative phase), and in the scaphoid fossa (positive phase). For P3 they are slightly displaced and more compact, in the cavum concha, in the cymba, and in the scaphoid fossa. In short, for this pinna it is difficult to disambiguate the P2 and P3 normal modes, from only their basic anti-node patterns.

Interestingly, the P2 pattern has a greater number of principal vectors pointing outwards to the surrounding air; this indicates a relatively larger proportion of energy loss at P2 resonance, which agrees well with the larger bandwidth of the second peak (cf. Fig. 2b). However, the overall patterns of acoustic flow for P2 and P3 appear similar, with the negative anti-node seemingly linked on either side with the two positive anti-nodes. To resolve the ambiguity, we next consider a more detailed analysis of the relative phases.

The left and right panels of Fig. 5 show the patterns for P2, after imposing thresholds on phase-angle differences in order to visualize only those quantities that have a *common phase*. The left panel visualizes only the positions at which $\phi_p < 45^\circ$ (positive-phase anti-node), $\phi_p > 135^\circ$ (negative-phase anti-node) and $\phi_v < 30^\circ$ (common-phase velocity-vectors). As a result, an independent resonance pattern is revealed involving energy oscillations only between the cavum concha and the cymba, while the third anti-node in the scaphoid fossa is clearly omitted.

In the right panel of Fig. 5, the thresholds on ϕ_p and ϕ_v were unchanged, with only the reference positions newly defined: $\mathbf{x}_{p\text{ref}}$ was selected deep inside the scaphoid fossa, and $\mathbf{x}_{v\text{ref}}$ was selected in the space between the scaphoid fossa and cymba. As a result, a second resonance is revealed

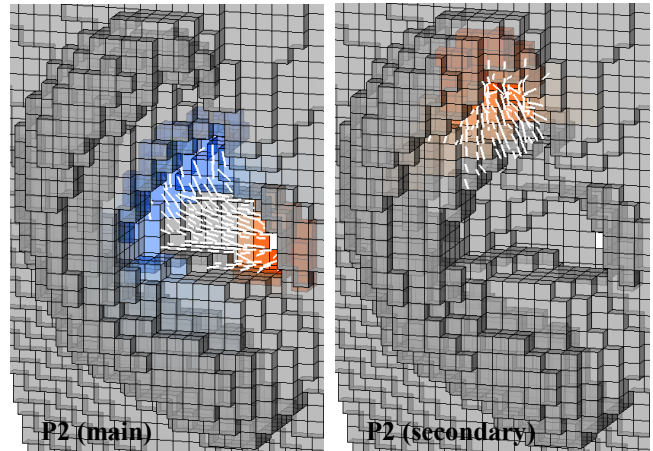


Figure 5. The two independent resonance patterns for P2 of the female pinna, as revealed by *common-phase* pressure anti-nodes and principal velocity-vectors. Left: main resonance. Right: secondary resonance.

involving only the scaphoid fossa.

Our phase analysis clearly indicates that there are two, acoustically decoupled resonance patterns that make up the P2 normal mode for the female pinna. In contrast, analysis of relative phases for P3 revealed only one resonance pattern, as already shown in the right panel of Fig. 4. Clearly for P3, the two positive anti-nodes in the concha and scaphoid fossa *synchronously* exchange energy with the negative anti-node in the cymba. The narrow bandwidth and high amplitude of the P3 peak (cf. Fig. 2b) are likely due to the strong acoustic coupling among those three pressure anti-nodes, resulting in a relatively low rate of energy loss to the surrounding air.

5. CONCLUSIONS

We described new methods for visualizing acoustic normal modes of human pinnae. Our methods extend the traditional visualization of pressure anti-nodes in mainly two new ways: (i) by including the essential features (strength and principal axis) of oscillatory air movements in the space between anti-nodes, calculated by PCA of velocity vectors; and (ii) by enabling separate visualization of independent resonances of a normal mode, via thresholding of relative phase-angles for both pressure and velocity.

Thanks to these methods, we were able to visualize a standard set of five normal modes for a male pinna; and to disambiguate the normal modes for P2 and P3 of a female pinna, revealing two independent resonance patterns for P2. Our signal processing and visualization methods should be widely applicable, to better understand the normal modes of any acoustically resonating structure. We plan to apply these methods to various human pinnae, with the aim of gaining a better understanding of the relations between individual pinna geometry and acoustic parameters required for spatial hearing.

6. REFERENCES

- [1] E.A.G. Shaw and R. Teranishi, "Sound pressure generated in an external-ear replica and real human ears by a nearby point source," *J. Acoust. Soc. Am.*, Vol.44 No.1, pp. 240-249, 1968.
- [2] Y. Kahana and P.A. Nelson, "Numerical modelling of the spatial acoustic response of the human pinna," *J. Sound and Vibration*, Vol.292, pp. 148-178, 2006.
- [3] P. Mokhtari, H. Takemoto, R. Nishimura, and H. Kato, "Acoustic sensitivity to micro-perturbations of KEMAR's pinna surface geometry," in *Proc. 20th Int. Cong. on Acoustics (ICA)*, Sydney, Australia, Paper 790, 8 pages, 2010.
- [4] H. Takemoto, P. Mokhtari, H. Kato, R. Nishimura, and K. Iida, "Mechanism for generating peaks and notches of head-related transfer functions in the median plane," *J. Acoust. Soc. Am.*, Vol.132 No.6, pp. 3832-3841, 2012.
- [5] P. Mokhtari, H. Takemoto, R. Nishimura, and H. Kato, "Preliminary estimation of the first peak of HRTFs from pinna anthropometry for personalized 3D audio," in *Proc. 5th Int. Conf. on Three Dimensional Systems and Applications (3DSA)*, Osaka, Japan, Paper S10-2, 3 pages, 2013.
- [6] P. Mokhtari, H. Takemoto, R. Nishimura, and H. Kato, "On individual differences in pinna-related transfer functions calculated by numerical simulation," in *Proc. 19th Int. Cong. on Sound and Vibration (ICSV)*, Vilnius, Lithuania, Paper 120, 8 pages, 2012.
- [7] P. Mokhtari, H. Takemoto, R. Nishimura, and H. Kato, "Optimum loss factor for a perfectly matched layer in finite-difference time-domain acoustic simulation," *IEEE Trans. Audio, Speech, and Lang. Process.*, Vol.18 No.5, pp.1068-1071, 2010.
- [8] P. Mokhtari, H. Takemoto, R. Nishimura, and H. Kato, "Efficient computation of HRTFs at any distance by FDTD simulation with near to far field transformation," in *Proc. Autumn Meeting of the Acoust. Soc. of Japan*, Fukuoka, Japan, Paper 1-8-12, pp. 611-614, 2008.
- [9] V.R. Algazi, R.O. Duda, D.M. Thompson, and C. Avendano, "The CIPIC HRTF database," in *Proc. IEEE Workshop on Applic. of Sig. Process. to Audio & Acoustics*, pp. 99-102, 2001.
- [10] P. Mokhtari, H. Takemoto, R. Nishimura, and H. Kato, "Computer simulation of KEMAR's head-related transfer functions: verification with measurements and acoustic effects of modifying head shape and pinna concavity," in Y. Suzuki *et al.*, Eds., *Principles and Applications of Spatial Hearing* (World Scientific), pp.205-215, 2011.
- [11] P. Mokhtari, H. Takemoto, R. Nishimura, and H. Kato, "Three-dimensional acoustic sensitivity analysis of pinna geometry at peaks of head-related transfer functions," in *Proc. Autumn Meeting of the Acoust. Soc. of Japan*, Toyohashi, Japan, Paper 3-1-17, pp. 861-864, 2013.